

A complete search for redshift $z \gtrsim 6.5$ quasars in the VIKING survey

Rhys Barnett¹*, S. J. Warren¹, N. J. G. Cross², D. J. Mortlock^{1,3,4},
X. Fan⁵, F. Wang⁶, and P. C. Hewett⁷

¹*Astrophysics Group, Blackett Laboratory, Imperial College London, London SW7 2AZ, United Kingdom*

²*Wide-Field Astronomy Unit, Institute for Astronomy, School of Physics and Astronomy,
University of Edinburgh, Royal Observatory, Blackford Hill, Edinburgh EH9 3HJ, UK*

³*Department of Mathematics, Imperial College London, London SW7 2AZ, UK*

⁴*Department of Astronomy, Stockholm University, Albanova, SE-10691 Stockholm, Sweden*

⁵*Steward Observatory, University of Arizona, 933 N. Cherry Avenue, Tucson, AZ 85721, USA*

⁶*Department of Physics, Broida Hall, University of California, Santa Barbara, CA 93106, USA*

⁷*Institute of Astronomy, University of Cambridge Madingley Road, Cambridge CB3 0HA, UK*

Accepted XXX. Received YYY; in original form ZZZ

ABSTRACT

We present the results of a new, deeper, and complete search for high-redshift $z > 6.5$ quasars over 977 deg^2 of the VISTA Kilo-Degree Infrared Galaxy Survey (VIKING) survey, that is sensitive out to $z \sim 9.3$. This exploits a new list-driven dataset providing aperture fluxes and uncertainties in all bands $ZYJHK_s$, for all sources detected by VIKING in J . We used the Bayesian model comparison (BMC) selection method of Mortlock et al., producing a ranked list of just 21 candidates. The sources ranked 1, 2, 3 and 5 are the four known $z > 6.5$ quasars in this field. Additional observations of the other 17 candidates, primarily DESI Legacy Survey photometry and ESO FORS2 spectroscopy, confirm that none is a quasar. This is the first complete sample (i.e., all candidates followed up) from the VIKING survey, and we provide the computed selection function. We also compute selection functions for samples produced by two other methods: colour cuts and minimum- χ^2 SED fitting. Comparison of the efficiency (fraction of candidates that are quasars) and the depth of the three methods leads to the following conclusions: i) BMC produces eight times fewer false positives than colour cuts, while also reaching 0.3 mag. deeper, ii) the minimum- χ^2 SED fitting method is extremely efficient but reaches 0.7 mag less deep than the BMC method, picking out only one of the four known quasars. By additionally following up BMC candidates rejected because their photometric SEDs have high χ^2 values, we identify a population of galaxies where very strong [OIII] $\lambda\lambda 4959, 5007$ emission in the Y band can mimic the colours of quasars, i.e., from Ly α and a blue continuum. This is a potential additional contaminant population in future searches for faint high-redshift quasars (such as in *Euclid*), not previously identified as such, and that requires better characterisation.

Key words: quasars: general

1 INTRODUCTION

Quasars at redshift $z > 6.5$ are useful probes of early supermassive black hole growth and the epoch of reionisation. Since the discovery of the first such quasar (Mortlock et al. 2011), the current tally of $z > 6.5$ quasars stands at almost fifty, with discoveries made using a wide range of near-infrared (NIR) surveys (Venemans et al. 2013, 2015b; Matsuoka et al. 2016, 2018a,b, 2019; Decarli et al. 2017; Koptelova et al. 2017; Tang et al. 2017; Reed et al. 2017, 2019; Wang et al. 2017, 2019; Songaila et al. 2018; Pons et al. 2019; Fan et al. 2019; Yang et al. 2019, 2020).

Discovering $z > 6.5$ quasars remains challenging, not least due to their space density, which declines strongly with increasing redshift. The decline of the number density of quasars brighter than a specific

absolute magnitude M_{1450} is often parametrised as

$$\rho(z, < M_{1450}) = \rho(z_0, < M_{1450}) 10^{k(z-z_0)}, \quad (1)$$

where z_0 is an arbitrary reference redshift. A comprehensive measurement of the QLF at $z \sim 6$ was made by Jiang et al. (2016), who used a complete sample of 47 SDSS quasars, $5.7 < z < 6.4$, measuring a rapid fall in quasar number density over $z = 5-6$, with $k = -0.72 \pm 0.11$. For $M_{1450} = -26$, they measure $\rho \sim 1 \text{ Gpc}^{-3}$ (comoving) at $z = 6$, corresponding to a surface density of approximately one object per 100 deg^2 .

In addition to the low numbers of quasars, selection of $z > 6.5$ quasars is severely hampered by contamination from intervening populations: cool stars and brown dwarfs (henceforth MLTs); and compact early-type galaxies (henceforth ETGs) at intermediate redshifts ($z \sim 1-2$), misclassified at low S/N as of stellar morphology. These populations are far more abundant than, and have similar

* E-mail: rhys.barnett09@imperial.ac.uk

NIR colours to, the target quasars (e.g., [Hewett et al. 2006](#))¹. Consequently, colour-selected samples of candidates are dominated by contaminants, especially as quasar searches move to lower S/N to maximise the number of discoveries. Because of this many searches have stopped after identifying the more obvious bright quasars, and have not persisted to the point of following up all candidates to produce a complete sample with a computed selection function, i.e., the measured completeness as a function of absolute magnitude and redshift. The measurement by [Wang et al. \(2019\)](#) of the space density at $z > 6.5$, using the DESI Legacy Survey ([Dey et al. 2019](#)) and Pan-STARRS ([Chambers et al. 2016](#)), is the only such analysis at these redshifts based on a complete sample. They measured $k = -0.78 \pm 0.18$ between $z = 6$ and $z = 6.7$, consistent with the rate of decline measured over $5 < z < 6$.

The main purpose of the current paper is to use the VISTA Kilo-Degree Infrared Galaxy (VIKING) survey ([Edge et al. 2013](#)) to produce a complete sample of $z > 6.5$ quasars (henceforth HZQs; high-redshift quasars), with a computed selection function, that reaches fainter absolute magnitudes and higher redshifts than the survey of [Wang et al. \(2019\)](#). Improving and extending measurements of the quasar luminosity function (QLF) to fainter luminosities and higher redshifts is an important aim, as such studies will constrain models of the formation and growth of supermassive black holes at early times (e.g., [Willott et al. 2010](#); [Jiang et al. 2016](#)), and are also important for designing future surveys for quasars at $z \sim 7$ and beyond, such as for *Euclid* ([Euclid Collaboration 2019](#)). The VIKING survey has already been searched using colour cuts, yielding four HZQs ([Venemans et al. 2013](#); [Wang et al. 2017](#)). To improve upon these previous searches we exploit a new list-driven photometric catalogue, which provides aperture-corrected aperture photometry in all five available bands $ZYJHK_s$ for every VIKING source detected in the J band ([Cross et al. 2014](#)). As explained in the next section this database has advantages for searches for HZQs.

To search the VIKING database we use an updated version of the Bayesian model comparison (BMC) technique developed by [Mortlock et al. \(2012\)](#). In a previous paper ([Euclid Collaboration 2019](#)) we compared two different search methods, namely BMC and minimum- χ^2 SED fitting (e.g., [Reed et al. 2017](#), applied to DES data). Using simulated datasets we showed that the BMC method is the more useful method as it reaches much deeper than the SED fitting method, while still being highly efficient. A third search method is the use of simple colour cuts, as applied by [Venemans et al. \(2013\)](#) in their search of the VIKING survey. Although we do not use the candidate lists, for the sake of comparison of the efficiency and depth of the methods we also produce candidate lists using the SED fitting and colour cuts methods. This extends the comparison of methods undertaken by [Euclid Collaboration \(2019\)](#), and has the advantage of using real data.

The paper is structured as follows. In Sect. 2 we give an overview of the VIKING survey, and the new list-driven dataset. In Sect. 3 we describe the BMC selection method used for the survey. We also detail the two other methods, SED fitting and colour cuts, that are used in the comparison of techniques. We present the results from our BMC HZQ search in Sect. 4. We compute the selection functions for the BMC search and for the other two methods in Sect. 5. In Sect. 6 we test that the models of the contaminating populations are rea-

sonable by creating a synthetic survey and comparing, for the three selection methods, the numbers of simulated candidates to the numbers of candidates found in the real data. We summarise in Sect. 7. All magnitudes and colours quoted are on the Vega system, unless otherwise stated. Where required we have cosmological parameters $h = 0.7$, $\Omega_M = 0.3$, and $\Omega_\Lambda = 0.7$.

2 VIKING SURVEY

VIKING is a medium-deep NIR survey covering $\sim 1300 \text{ deg}^2$ in five broadband filters – Z, Y, J, H and K_s – with the VISTA telescope. VIKING datasets are named by the release date. The list-driven photometry database used here is based on the dataset 20160406. This contains 782 framesets, which has a footprint covering a total area of 988.7 deg^2 .

The standard VIKING catalogues are formed by merging lists of objects detected in each filter. The subsequent list-driven photometry ([Cross et al. 2014](#)) is motivated by the fact that the majority of HZQs will be too faint in the Z band to be detected, as a result of absorption by neutral hydrogen along the line of sight (e.g., [Barnett et al. 2017](#)). Consequently, the Z band will only provide a flux limit. For such sources, a flux measurement provides much more information than an upper limit ([Mortlock et al. 2012](#)). Our new list-driven catalogue is produced by performing aperture photometry in each band at the position of every object that is detected in the VIKING J band, and applying an aperture correction appropriate for a point source. Further details of the creation of the list-driven catalogue will be provided in a forthcoming paper (Cross et al., in prep.; see also [Ross & Cross 2020](#)).

The photometric depths vary across the survey. The distributions of depths in the different bands are plotted in Fig. 1. Here depth is quantified by the total magnitude of a point source detected at 5σ in a $2''$ diameter aperture. The median 5σ depths are $(Z, Y, J, H, K_s) = (22.1, 20.3, 20.9, 19.8, 19.2)$. These depths are some 1.5 mag. deeper than the UKIDSS data used by [Wang et al. \(2019\)](#).

Regions close to bright stars are excised from the dataset as we found that the VIKING photometry of sources is unreliable in these locations. We observe an excess of candidates near bright stars, which are therefore clearly false positives. The size of the region affected increases with the brightness of the star. We used the 2MASS catalogue ([Skrutskie et al. 2006](#)) to quantify this, as the bright stars are saturated in VIKING. We drilled holes around stars brighter than $J = 11$, with a radius R dependent on the 2MASS magnitude according to $R = 20''(11 - J_{2\text{MASS}})$. There are 4.3×10^4 bright stars with $J_{2\text{MASS}} < 11$ in the VIKING footprint and we remove 12.2 deg^2 from the survey, leaving an effective area of 976.5 deg^2 .

3 HIGH REDSHIFT QUASAR SELECTION

In this section we provide the details of our search for HZQs that uses the BMC method. In Sect. 3.2 we also list the details of the SED fitting and colour cuts techniques that are used in our comparison of methods. The BMC and SED fitting methods both require model colours of the contaminating populations. The BMC method additionally requires models of the surface density, as a function of apparent magnitude, of the contaminating populations and of the quasars. The populations modelled are the same as we used in the *Euclid* study ([Euclid Collaboration 2019](#)), but adapted specifically for VIKING data, taking into consideration the different filter transmission curves and image quality. We have relegated the section on

¹ A further known class of contaminant which we do not explicitly treat in this work are extreme FeLoBALs (e.g., [Hall et al. 2002](#)), where strong MgII absorption can produce a sharp continuum break. These are considerably less common than MLTs and ETGs, but more common than $z > 6.5$ quasars.

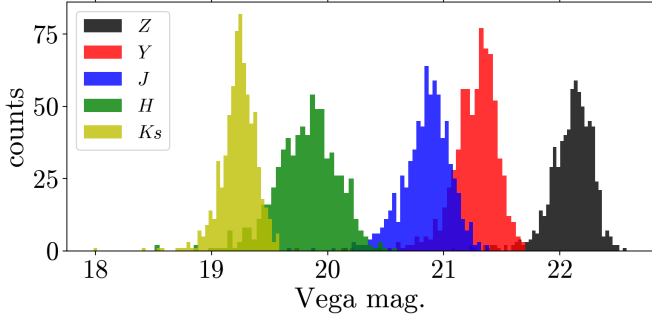


Figure 1. Distribution of 5σ frameset depths in each VIKING band.

population modelling to the Appendix, Sect. B. The colours of the three populations, quasars, MLTs, ETGs, or plotted in Fig. 2, showing the $Z - Y$, $Y - J$ and $J - H$ colours, and also plotting the colours of the four known VIKING HZQs. At high S/N the three populations are easily mutually distinguishable. At low S/N extreme outliers from the two contaminating populations, which outnumber quasars by orders of magnitude, can have the same observed colours as the target quasars.

3.1 Candidate selection using Bayesian Model Comparison

3.1.1 Initial cuts

To target HZQs, before applying the BMC algorithm we implement the following cuts:

- (i) $S/N_J \geq 4$. Given that our list-driven catalogue requires a J band detection, very few sources are removed by this step. We do not have an equivalent requirement in Y , which means our sensitivity in redshift extends to $z \sim 9.3$. However, in a survey of the depth and area of VIKING the predicted yield is extremely small at such high redshift.
- (ii) The particular field was observed in all three bands ZYJ .
- (iii) $S/N \geq 4$ in one additional band Y , H or K_s . In practice this ensures that a J -band detection corresponds to a real source.
- (iv) $S/N_Z < 4$, or $Z - Y \geq 1.5$.
- (v) $-4 < \text{MergedClassStat} < 2$. The parameter `MergedClassStat` (MCS) is a morphology statistic in VIKING, which we use to exclude identifiably extended sources.
- (vi) Not on detector 16. Flat-fielding is not accurate for this CCD due to a time-varying quantum efficiency and many detected sources are spurious. A flag is automatically applied to VIKING sources from this detector (Cross et al. 2012). The exclusion of detector 16 is accounted for in the quoted survey area and corresponds to a reduction in area of 6%.

These selection criteria are very broad, with the goal of maximising the discovery space of HZQs. The only explicit colour cut is in item 4. It is common to apply a higher S/N threshold than we have in item 1. The very low S/N threshold applied is possible because the BMC method utilises the photometric uncertainties in an optimal way. One $z > 6.4$ quasar in VIKING, listed with $z = 6.51$ by Chen et al. (2017), but revised to $z = 6.44$ by Decarli et al. (2018), lies above, but close to the $Z - Y$ cut. This indicates that the colour cut lies close to $z = 6.5$. This source is also excluded by the colour cuts applied by Venemans et al. (2013), described below. Our cut on $Z - Y$ is slightly redder than that used by Venemans et al. (2013), which we

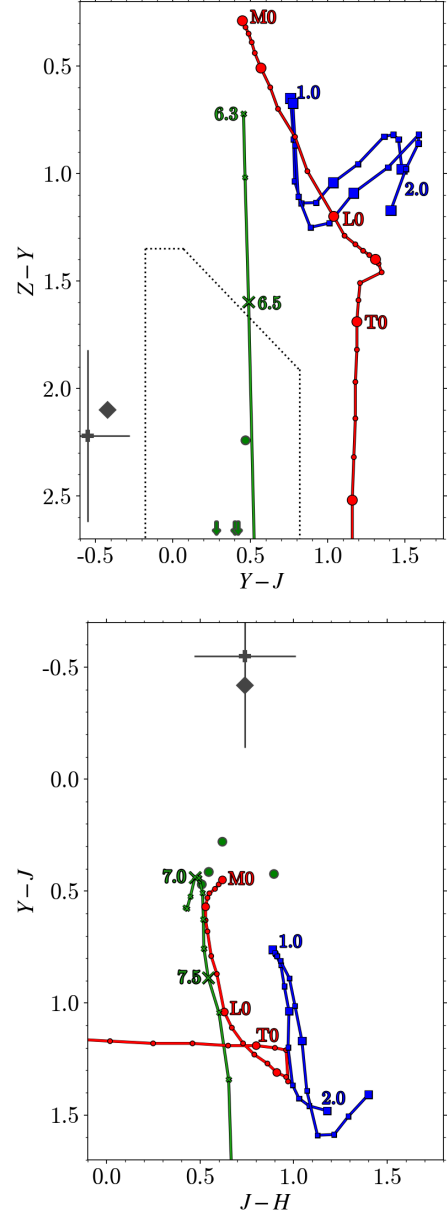


Figure 2. Colour-colour diagrams of relevant populations. *Green tracks (crosses)*: HZQ model colours as a function of redshift, spacing $\Delta z = 0.1$. *Red tracks (circles)*: model MLT colours for each spectral type. *Blue tracks (squares)*: ETGs ($z_f = 3$ and $z_f = 10$), spacing $\Delta z = 0.1$. Green circles are the known VIKING HZQs. The grey plus-sign indicates the emission-line galaxy VIK J1459-0321 (Sect. 4.1). The grey diamond indicates the average colours of the high- χ^2 rejected candidates, (Sect. 4.1). *Upper*: ZYJ colours. Colour cuts are shown as black dotted lines. Three of the known HZQs have $Z - Y > 3$, and are indicated using arrows. *Lower*: YJH colours.

found helped reduce the number of false positives in our search with BMC.

As detailed below, for sources identified by the BMC method as candidate quasars, we apply an additional cut $\chi^2_{\min} < 11$. The quantity χ^2_{\min} is the goodness of fit of the quasar model that provides the best fit to the photometry.

3.1.2 Bayesian model comparison method

We use an extension of the BMC technique proposed by [Mortlock et al. \(2012\)](#). The extended method is additionally described in detail by [Euclid Collaboration \(2019\)](#), so we only recap the main points here.

The method works by determining a ‘weight’ for each population under consideration, with a population posterior probability given by the ratio of those weights. In our search for quasars, denoted q , where we have assumed two contaminating populations, MLTs, s , and ETGs, g , we define the probability that a source is a quasar, P_q , given photometric data \mathbf{d} as:

$$P_q \equiv p(q|\mathbf{d}) = \frac{W_q(\mathbf{d})}{W_q(\mathbf{d}) + W_s(\mathbf{d}) + W_g(\mathbf{d})}. \quad (2)$$

The individual weights for a population are calculated by combining all available photometric data for a source, with the surface density of the population, which serves as the prior. For a given source, a particular population weight measures the relative probability that the source would have the measured photometry in all bands, characterised by the model colours for that population, weighted by surface density as a function of apparent magnitude. [Mortlock et al. \(2012\)](#) applied the method to the case of two populations: quasars and M stars; here we have extended the method to three populations. Additionally, the MLT population is now divided into a set of sub-populations, namely the individual spectral types from M0 to T8. This approach to the cool dwarf population is similar to that of [Pipien et al. \(2018\)](#), who developed models for each spectral type L0–T9 in a search for high-redshift quasars in the Canada-France High- z Quasar Survey in the Near-Infrared.

Explicitly, individual weights for each type, $W_t(\mathbf{d})$, are given by

$$W_t(\mathbf{d}) = \int \rho_t(\boldsymbol{\theta}_t) p(\mathbf{d}|\boldsymbol{\theta}_t, t) d\boldsymbol{\theta}_t, \quad (3)$$

where $\boldsymbol{\theta}_t$ is the set of parameters describing each population. The two terms in the integral in Equation 3 are respectively the surface density function, and a Gaussian likelihood function based on model colours, which is written in terms of (linear) fluxes (as opposed to magnitudes).

The chosen threshold value of P_q effects a balance between contamination and completeness. A value $P_q > 0.1$ worked well for the UKIDSS LAS high-redshift quasar survey ([Mortlock et al. 2012](#)). However, we found the number of candidates rises steeply for VIKING as the threshold is lowered from $P_q = 0.15$ to $P_q = 0.1$, with only a small associated change in the simulated selection function, and hence the predicted quasar yield. The implication is that the lower P_q threshold simply allows more contaminants into the sample, to no significant benefit. Therefore in this work we select candidates with $P_q > 0.15$.

In the Appendix, Sect. A, we detail a slight modification to the selection procedure which we applied to sources which have both a primary and secondary entry in VIKING as a result of the VISTA observation strategy (i.e., the source is duplicated in the catalogue).

3.2 Candidate selection using other methods

3.2.1 SED fitting

The second method that we consider is minimum- χ^2 SED fitting. [Reed et al. \(2017\)](#) applied such a method to a combination of DES, VHS and WISE data, discovering eight bright ($z_{\text{AB}} < 21.0$) $z > 6$ quasars, including one source with $z = 6.50$. The method was also compared to BMC in [Euclid Collaboration \(2019\)](#). This method is

applied to the same sample that the BMC method is applied to, i.e., after the initial cuts enumerated in Sect. 3.1.2.

The method works by fitting a range of quasar and contaminant model SEDs to the measured fluxes of a source, minimising the reduced χ^2 value, χ_{red}^2 . We calculate the χ_{red}^2 value for a given model SED m as follows:

$$\chi_{\text{red},m}^2 = \frac{1}{N_b - 2} \sum_b \left(\frac{\hat{f}_b - s_{\text{best}} f_{m,b}}{\hat{\sigma}_b} \right)^2, \quad (4)$$

where \hat{f}_b and $\hat{\sigma}_b$ are the measured flux and its uncertainty in band b , $f_{m,b}$ is the (unnormalised) model SED flux in band b , and s_{best} is the normalisation that minimises χ^2 . We have $N_b - 2$ degrees of freedom as there are two parameters under consideration: the normalisation of a single model, and the particular model being fitted, selected from a range of models (e.g., [Skrzypek et al. 2015](#)). That is to say, for the quasars and early-type galaxies the second parameter is redshift, $\Delta z = 0.05$, while for the MLT dwarfs, which form a continuous sequence, the second parameter is spectral type.

We use the model colours detailed in the Appendix, Sect. B, to produce quasar and contaminant SEDs, and fit them to the fluxes of each source, following Eq. (4). We keep the single best fitting quasar (q) model and contaminant (c) model, with respective χ_{red}^2 values $\chi_{\text{red},q(\text{best})}^2$ and $\chi_{\text{red},c(\text{best})}^2$. Following [Reed et al. \(2017\)](#), we apply two cuts to the χ_{red}^2 values to retain a source (see Figure 15 of that work). We firstly require $\chi_{\text{red},c(\text{best})}^2 > 10$, i.e., the data are a bad fit to all contaminant models. We additionally require the ratio $\chi_{\text{red},c(\text{best})}^2 / \chi_{\text{red},q(\text{best})}^2 > 3$, i.e., the data are fit substantially better by a quasar SED than any contaminant model.

3.2.2 Colour cuts

The final method we use in this paper is the ‘conservative’ set of colour/magnitude cuts used to select quasars from 332 deg² of VIKING by [Venemans et al. \(2013\)](#). The selection criteria, transformed from the AB photometric system used by them to the Vega system used here, are the following:

- (i) $Z - Y > 1.35$, or undetected in Z (VIKING).
- (ii) $S/N_Z < 3$ or $Z - Y > 1.3 + 0.75(Y - J)$.
- (iii) $-0.2 < Y - J < 0.8$.
- (iv) $0.7 < Y - K_s < 2.5$, or unmeasured in K_s .
- (v) $\sigma_Y(\text{VIKING}) < 0.15$. This requirement limits the search to redshifts $z < 7.5$, in contrast to the other two search methods used here.
- (vi) Not on detector 16.

A source must satisfy all criteria to be accepted. In their search, [Venemans et al. \(2013\)](#) also undertook their own aperture photometry on the images, and additionally applied the above cuts to the repeat photometry. Since we do not have access to their software, we use the list-driven photometry to emulate this process, i.e., we apply the cuts first to the standard VIKING photometry, then additionally to the list-driven photometry. In the first stage we also apply the morphological cut $p\text{Galaxy} < 0.95$ used by [Venemans et al. \(2013\)](#).

4 RESULTS: $z > 6.5$ QUASAR CANDIDATES

We present the BMC candidate list, and the results of follow-up observations, in Sect. 4.1. We did not discover any new quasars; however, the four known quasars in the VIKING area are easily

recovered. In Sect. 4.2 we outline the candidate lists produced using the other two methods. As noted above these are only for the purposes of comparing the efficiency and depth of the three different selection methods.

4.1 Results from Bayesian model comparison

Applying our first cuts to the full VIKING survey (Sect. 3.1), we have an initial sample of 3.6×10^5 sources, to which we apply the BMC method. All candidates satisfying $P_q > 0.15$ were then checked on the VIKING images. At this stage we were left with a number of candidates with $P_q > 0.15$ that nevertheless have SEDs very different to the SEDs of quasars. For each candidate we determined the best-fit quasar SED, by $\min-\chi^2$. For sources with measurements in all five bands $ZYJHK_s$ this fit has three degrees of freedom, so we rejected all candidates with $\chi^2_{\min} > 11$. For three degrees of freedom, this cut corresponds to a 1% probability, i.e., in principle we include 99% of quasars with this cut. We removed 21 candidates in this way. The nature of the sources eliminated by this cut is discussed later in this section. The final candidate list is provided in Table 1, and contains 21 sources. The Table lists the coordinates, the value of P_q , the value of χ^2_{\min} , and z_{best} , the redshift of the best-fit SED. Ranking the candidates by P_q , the four known HZQs are ranked numbers 1, 2, 3, 5.

Since we want a complete sample we must confirm whether or not any of the remaining 17 candidates is a quasar. At redshifts $z > 6.5$, flux shortward of the quasar Ly α emission line is almost completely absorbed, with at most some residual transmission redward of Ly β which lies at $\lambda > 770$ nm (see e.g., Barnett et al. 2017). Therefore if a candidate is a HZQ, there will be negligible flux in the g and r photometric bands, which lie blueward of $\lambda 700$ nm. (We therefore ignore the possibility of gravitational lensing by an intervening galaxy that magnifies the quasar image(s) and directly contributes optical flux, see Fan et al. 2019.) We matched our candidates to imaging data from the DESI Legacy Survey, the VST ATLAS survey (Shanks et al. 2015), the Kilo-Degree Survey (KiDS, de Jong et al. 2017), and Pan-STARRS, and eliminated any candidates clearly detected in either of these bands². The images (survey and photometric band) used to eliminate any candidate are listed in the final column of Table 1.

We obtained spectra to confirm the nature of the remaining five objects. One of these, VIK J140811.2–024439.4, was observed using Magellan FIRE in June 2017. The other four candidates were observed with the ESO FORS2 instrument between 11th November 2018 and 18th March 2019, as well as one additional source VIK J021941.3–272533.8 that was only later detected in a r image. The six spectra all display continua steeply and smoothly rising towards longer wavelengths, characteristic of L and T dwarfs, without the continuum break or Ly α emission line characteristic of HZQs. Accordingly these sources were also eliminated. In this way all 17 candidates were eliminated, meaning no new quasars were discovered. By this means, the four previously known quasars now form a complete sample.

4.1.1 The nature of $\chi^2_{\min} > 11$ sources

A number of candidates have acceptable values of $P_q > 0.15$ but the best fit quasar model is a very bad fit, with $\chi^2_{\min} > 11$. This suggests

² In principle this additional optical photometry should be incorporated into the BMC calculation. However, for our search optical data were not available at the time the candidate list was finalised.

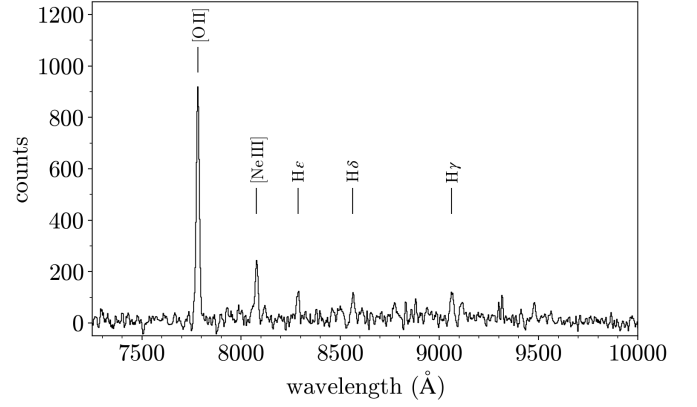


Figure 3. FORS2 spectrum of VIK J1459–0321, a $z = 1.087$ emission line galaxy selected as a HZQ candidate using BMC, with $P_q = 0.20$. The spectrum has not been flux calibrated.

that the object is not a member of any of the three populations considered, and may indicate the presence of another contaminating population. In Table 1 we list the objects in this category with $11 < \chi^2_{\min} < 40$. To investigate the nature of this population we again matched the sources to the deep optical surveys previously cited. Most are detected in the r band. Two sources were not detected in g or r and we obtained spectra of these. Their spectra have the characteristics of L or T dwarfs. Conceivably they are subdwarfs, but this cannot be confirmed without much longer integrations. We also targeted a source detected in r with one of the smallest values of χ^2_{\min} in this group. The spectrum of this source, VIK J145914.6–032129.11 (VIK J1459–0321), is plotted in Fig. 3. It is an emission line galaxy (ELG) with $z = 1.087$.

The colours of this source are plotted in Fig. 2, where it can be seen that the source is very blue in $Y - J$. Given the redshift of the source, the emission lines H β and [OIII] $\lambda\lambda 4959, 5007$ lie in the Y band, but off the red end of the spectrum plotted in Fig. 3. From the spectrum it is clear that the Balmer lines are weak, so the very blue $Y - J$ colour must be caused by very strong [OIII] $\lambda\lambda 4959, 5007$ emission. The strength of the high-ionisation [NeIII] line compared to the Balmer lines suggests this object is likely to be an AGN. Also plotted in Fig. 2 are the average colours, and scatter, of the nine sources in the high- χ^2 reject category that are visible in g or r . These are consistent with the colours of VIK J1459–0321, suggesting that they may all be ELGs at similar redshifts. While these objects are easily distinguished from quasars, by their high χ^2 values, similar sources with somewhat weaker emission lines might have less blue $Y - J$ colours, and so smaller values of χ^2 . It is possible that some of the actual candidates, i.e., objects with $\chi^2 < 11$, detected on r , are also ELGs.

This population of ELGs, with very strong [OIII] $\lambda\lambda 4959, 5007$ emission, is discussed in the literature (e.g., Atek et al. 2011; Hayashi et al. 2018), but this is the first time it has been pointed out as a potential contaminating population for searches for HZQs. The *Euclid* search for HZQs (*Euclid* Collaboration 2019) will reach deeper and over a larger area than the VIKING survey, although at higher redshifts. As described in the *Euclid* paper we made an explicit search of the deep COSMOS data (Laigle et al. 2016) for an additional contaminating population, failing to find any such sources over the 1.5 deg^2 of the COSMOS field, but the *Euclid* wide survey will cover an area 10 000 times larger. Therefore further analysis and better

Table 1. VIKING HZQ candidates from the BMC method. Follow-up imaging (g or r) and spectroscopic (FORS2/FIRE) observations are listed in the final column. Here ‘Legacy’ means the DESI Legacy Survey. The asterisked probabilities were calculated on the basis of combining primary and secondary VIKING photometry for those sources (see Appendix Sect. A).

	α	δ	P_q	χ^2_{\min}	z_{best}	notes
Known HZQs	01:09:53.1	−30:47:26.3	0.97	0.6	7.00	$z = 6.8$, Venemans et al. (2013)
	03:05:16.9	−31:50:55.9	1.00*	2.1	6.55	$z = 6.6$, Venemans et al. (2013)
	10:48:19.1	−01:09:40.3	1.00	4.5	6.60	$z = 6.6$, Wang et al. (2017)
	23:48:33.3	−30:54:10.2	1.00*	2.3	7.00	$z = 6.9$, Venemans et al. (2013)
Candidates	00:03:51.3	−31:24:00.3	0.21	1.9	6.65	FORS2
	00:27:57.6	−30:02:19.7	0.20	1.9	6.45	Legacy r
	00:45:39.7	−34:28:02.3	0.17	0.1	7.45	FORS2
	00:58:42.9	−28:52:06.2	0.42	3.3	6.50	Legacy r
	01:00:23.2	−28:55:36.5	0.19	1.5	6.55	Legacy r
	01:21:52.0	−28:00:18.4	0.99	5.8	6.40	Legacy r
	01:40:12.3	−27:54:04.7	0.17	1.3	6.50	Legacy r
	01:46:30.5	−30:11:51.1	0.63	0.4	7.40	FORS2
	02:19:41.3	−27:25:33.8	0.38	5.9	7.00	Legacy r , FORS2
	03:13:16.8	−30:59:21.0	0.77*	6.9	6.45	Legacy r
	08:59:02.9	−01:36:02.5	0.25	2.4	6.45	Legacy r
	12:05:47.1	+01:52:54.3	0.37*	2.1	6.50	Legacy r
	14:08:11.2	−02:44:39.4	0.29	1.6	6.60	FIRE
	22:02:09.6	−28:19:51.0	0.27	1.1	7.50	FORS2
	22:25:11.2	−27:23:29.7	0.16	3.6	6.45	Pan-STARRS r
	22:39:54.6	−27:12:18.2	0.64	1.6	6.45	ATLAS r
	23:24:17.9	−30:12:12.4	0.52	5.4	6.45	KiDS r
Rejects $11 < \chi^2_{\min} < 40$	01:13:32.1	−30:08:45.6	0.91	18.4	6.50	Legacy r
	01:27:59.1	−33:02:57.1	0.31	25.1	6.45	Legacy r
	02:16:04.3	−32:58:58.7	0.39	31.4	7.00	FORS2
	02:16:23.4	−32:07:40.5	0.99	32.3	6.55	FORS2
	11:48:27.8	+02:53:51.9	0.53	19.8	6.45	Legacy r
	12:25:39.6	+02:31:27.8	0.47	14.4	6.45	Legacy r
	12:45:09.3	−01:40:23.4	0.62	27.4	6.50	ATLAS g
	12:51:50.1	+02:50:16.2	0.98	35.0	6.40	Legacy r
	14:45:21.0	+02:00:58.4	0.99	36.3	7.00	Legacy r
	14:59:14.6	−03:21:29.1	0.20	22.0	6.50	Legacy r , FORS2; ELG, Fig. 3
	23:04:16.1	−34:52:30.8	0.20	24.2	6.45	ATLAS g

characterisation of this ELG population is needed, to feed into HZQ selection with *Euclid*. It may be that the much better imaging quality of *Euclid* compared to VIKING will allow the ELG population to be eliminated from quasar searches as extended sources, or that the complementary ground-based optical imaging data will be deep enough to detect these sources, in r or i , and so eliminate them in that way.

A further known contaminant in $z > 6.5$ quasar surveys are FeLoBALs (Hall et al. 2002), although none of the objects for which we obtained a spectrum in this work is an example. FeLoBALs are best eliminated by deep photometry in the optical bands, and it is conceivable that some of our objects detected in r fall into this category.

4.2 Candidate lists from other methods

We applied the SED fitting criteria to the same initial sample of 3.6×10^5 sources as in Sect. 4.1. After checking the VIKING images of all candidates we were left with only two candidates, of which one is the $z = 6.9$ quasar listed in Table 1, and the other is one of the BMC candidates, which we excluded on the basis of a DESI Legacy Survey detection. The other three known quasars are excluded as the photometry is well-enough fit by a contaminant model. This implies that the SED fitting method is very efficient, but only picks out the most obvious sources. In our analysis for *Euclid* (Euclid Collaboration 2019), we investigated whether tuning the selection parameters for

SED fitting could improve the completeness. However, in that work we found relaxing the cuts slightly resulted in a threefold increase in contamination, for only a 10% increase in the predicted number of quasars found. We concluded that it was difficult to improve the depth significantly without the number of candidates rapidly rising.

Using the colour cuts, and after checking all candidates in the VIKING images, we are left with a total of 199 good HZQ candidates. We recover the four known quasars as well as five BMC candidates listed in Table 1 (all of which have detections in the r band). We find a further 124 candidates which are not selected by the BMC algorithm because $P_q < 0.15$. Finally, there are 66 additional candidates which were not checked using BMC, as they lie above the $Z - Y$ cut applied to produce the initial sample used in the BMC method. The surface density of the 199 candidates, from 977 deg^2 , is 0.20 deg^{-2} . Venemans et al. (2013), selected 43 candidates from 332 deg^2 , or 0.13 deg^{-2} , so our methods are reproducing theirs reasonably closely.

Considering the colour range in common, the BMC method produces 17 false positives. Colour cuts produce 129 candidates in addition to the known quasars. Considering the high probabilities of the confirmed quasars it can be assumed that nearly all the 129 candidates are false positives, so on this basis we find colour cuts produce eight times as many false positives as the BMC method.

5 SELECTION FUNCTIONS

In this section we compute the quasar selection functions for the three selection methods, i.e., we compute the probability that a quasar of given absolute magnitude and redshift, and spectral type, would be selected by each method. We start with a grid in luminosity/redshift space, over which we simulate large numbers of quasars. Although the selection algorithm employs only a single quasar spectral type, one with typical properties, quasars in reality have a range of emission-line strengths, and continuum slopes. Therefore we must measure the detection probability over the full range of spectral types. The final selection function weights the detection probabilities by the assumed fractions of the different spectral types.

We employ nine different spectral types, corresponding to all combinations of three different line strengths and three continuum slopes. Further details of the models are provided in *Euclid* Collaboration (2019). We produce realistic list-driven fluxes for these sources using our model colours (Appendix, Sect. B1), and add Gaussian noise based on the distribution of frameset depths in each band (Fig. 1). We additionally simulate the process of detection in the J band, which determines whether a real source will appear in the list-driven catalogue. The way the detection process is modelled is described in the Appendix, Sect. C. This is relevant for the BMC method, which reaches very deep.

We determine the final quasar selection functions by recording the fraction of simulated HZQs that pass the selection criteria for each method, considering every step in the selection process, i.e., following the procedures detailed in Sect. 3. The three selection functions are plotted in Fig. 4.

There is a sharp cut-off in sensitivity to quasars below $z = 6.5$ for all three methods. Colour cuts are insensitive to quasars at $z \gtrsim 7.6$, beyond which the $\text{Ly}\alpha$ break is sufficiently redshifted that HZQs become too faint in the Y band to be selected. By contrast there is no Y -band S/N requirement for the other two methods (a source with a 4σ flux measurement in any of YHK_s will be accepted), and quasars could in principle be recovered up to $z \sim 9.3$. For the BMC and SED fitting methods there is a noticeable decline in selection efficiency over the redshift interval $7.5 < z < 8.0$. Over this redshift range, HZQs fainter than $J \sim 19$ begin to be misclassified as MLTs, as a result of the very similar colours of the two populations.

Over the redshift range in common to the three methods, the BMC method reaches deepest, followed by colour cuts, and then SED fitting. To quantify the relative performance of the three HZQ selection methods, we integrate the QLF over the quasar selection functions in Fig. 4, to determine a ‘predicted yield’ of HZQs using each method. We use the Jiang et al. (2016) QLF measured at $z = 6$, and evolve it in redshift using the value $k = -0.78$ measured by Wang et al. (2019), assuming this value applies at all redshifts $z > 6$. We plot the predicted numbers in redshift bins in Fig. 5. The total counts are 6.4, 2.4, 4.4 for the BMC, SED fitting, and colour cuts methods. Although the BMC and SED-fitting methods have sensitivity to $z > 8$ quasars, in practise this is not of great interest as the predicted numbers are negligible for the assumed luminosity function evolution. The tally of four detected quasars using BMC is effectively a -1σ deviation from the predicted counts³. The implication of the results is that the rate of decline of the luminosity function with redshift is slightly

steeper than found by Wang et al. (2019). In a future paper we will combine our dataset with that of Wang et al. (2019), to carry out a full analysis of the redshift evolution at $z > 7$.

To quantify the relative depths of the three selection methods we consider the redshift range $6.6 < z < 7.0$. We sum the predicted counts over this redshift range for each method. We then similarly integrate the evolving luminosity function, assuming 100% completeness, to find the depth that matches the counts for each method. The effective depths of the BMC, SED fitting, and colour cuts methods are respectively $M_{1450} = -25.0, -25.7, -25.3$. This implies that the BMC method reaches 0.3 mag. deeper than colour cuts, and 0.7 mag. deeper than SED fitting.

6 CONTAMINANT SIMULATIONS

As a test of the modelling process, and therefore of the reliability of the selection functions, we created a synthetic survey using the population modelling and selection apparatus already described. We ran our selection methods on the synthetic survey and compared the numbers of synthetic candidates to the numbers of actual candidates. Our models for the contaminants specify the surface density as a function of apparent magnitude and colour. The synthetic survey accounts for the varying depths across the VIKING survey by simulating sources for every frameset. We simulate sources down to a magnitude fainter than the 5σ limit of each frameset in order to correctly model the possibility that faint sources are scattered by flux errors to brighter than the detection limit. For both contaminating populations we use the model colours to determine true fluxes in each band, and then add Gaussian noise based on the frameset depth. We discard sources that are not detected in the J band, and in the case of ETGs we reject sources on the basis of the morphology cut (Appendix Sect. B3). The resulting synthetic survey contains $\sim 1.5 \times 10^6$ MLTs, and $\sim 4 \times 10^5$ ETGs (many having been removed by the morphology cut). We gauge the predicted contamination by applying our selection methods to this sample.

For the BMC method we predict contamination by 29 sources, as compared to the 17 contaminants found (effectively a -2σ fluctuation), and for SED fitting we predict one contaminant which matches the one found. These numbers are in very close agreement, providing confidence in the models used and therefore in the accuracy of the computed selection functions. However, we note that our idealised simulations do not incorporate the possible ELG population discussed in Sect. 4.1, and that at present it is unclear what fraction of the contaminants are ELGs.

We cannot fully simulate the colour cuts method using simulations. Recall (Sect. 3.2.2) that Venemans et al. (2013) required an object to meet their selection criteria both in the catalogue data and in their own repeat photometry. While we could emulate this in the candidate selection, we cannot do this in the simulation. Because of this the simulation is expected to overestimate the number of candidates, and this is indeed the case, but not by much. Applying the colour-cut criteria to the simulations we select 472 HZQ candidates. In the actual data we selected 199 candidates using colour cuts. These results again indicate the models are providing a good representation of the contaminant populations, and therefore that the selection functions are reliable.

³ To further check the consistency of the BMC selection function and VIKING HZQ sample we draw 1×10^5 fake quasar samples from the product of the selection function and the QLF. We calculate the log likelihood of each (Marshall et al. 1983). The log likelihood of the VIKING sample is consistent with the resulting distribution.

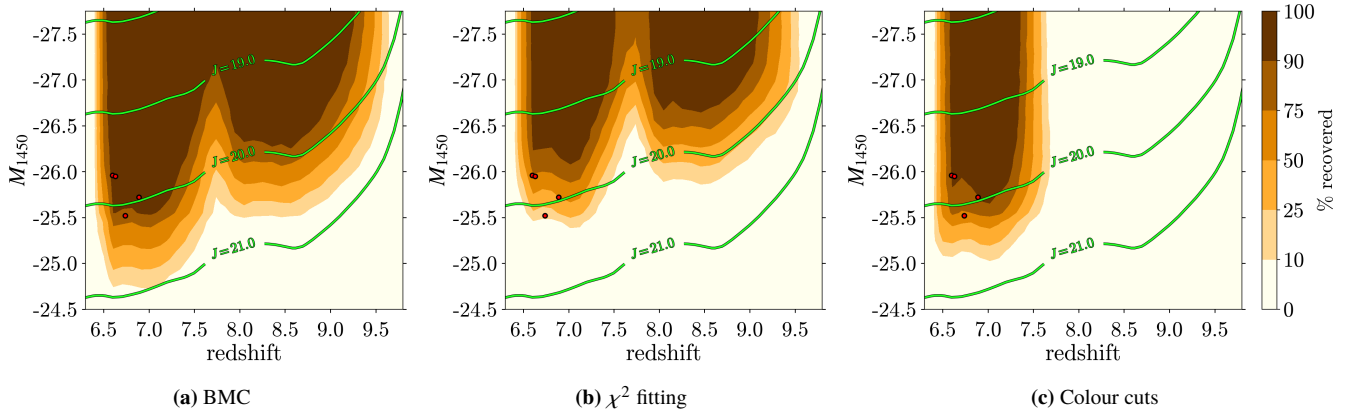


Figure 4. Selection functions for the three different selection methods. Circles indicate the four published VIKING HZQs (Venemans et al. 2013; Wang et al. 2017). Contours of constant apparent magnitude, computed using k -corrections determined for an average quasar SED, are indicated in green.

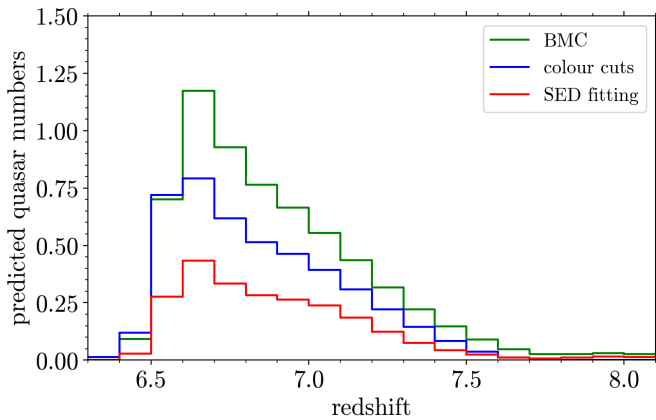


Figure 5. Predicted HZQ yield as a function of redshift for each selection method, produced by multiplying the selection functions in Fig. 4 by the Jiang et al. (2016) QLF, evolved beyond $z = 6$ using $k = -0.78$.

7 CONCLUSIONS

In this paper we have presented a search for redshift $6.5 < z < 9.3$ quasars over 977 deg^2 of the VIKING survey. We have exploited a new list-driven dataset, which provides fluxes and uncertainties for all J -detected VIKING sources, in all available photometric bands $ZYJHK_s$. We searched the database using a modification of the BMC method of Mortlock et al. (2012), and produced a sample of 21 candidate quasars $z > 6.5$. This candidate list includes the four previously discovered $z > 6.5$ quasars in this field.

We have followed up the additional 17 candidates and confirmed that none are quasars. The sample and the selection criteria define a complete sample and allow us to compute the survey selection function for VIKING for the first time. The survey reaches some 1.5 mag. deeper than the sample of Wang et al. (2019), the only other complete sample at these redshifts. Previous searches of VIKING (Venemans et al. 2013; Venemans et al. 2015a) covered a smaller area, were not as deep, and were incomplete in that they did not follow up all candidates.

We also undertook a comparison of three different selection methods, BMC, SED fitting and colour cuts. We found that the BMC method is the best. It reaches 0.3 mag. deeper than the colour cuts

method, while the number of false positives is a factor of eight smaller. The BMC method reaches 0.7 mag. deeper than the SED-fitting method, which only finds one of the four known quasars in this field.

We find evidence for a population of emission line galaxies with strong $[\text{OIII}]\lambda\lambda 4959, 5007$ emission, which could potentially contaminate future surveys for high-redshift quasars such as with *Euclid*, and therefore needs to be better characterised.

In a forthcoming publication we will use the new complete sample and associated selection function to refine the estimated rate of decline in quasar space density over the interval $6 < z < 7.5$.

ACKNOWLEDGEMENTS

Based on observations collected at the European Organisation for Astronomical Research in the Southern Hemisphere under ESO programme(s) 0102.A-0848(A). We are very grateful to Christian Hummel our ESO support astronomer for extensive help in the preparation of the FORS2 spectroscopic observations. We thank Sophie Reed for useful discussions. This work was supported by grant ST/N000838/1 from the Science and Technology Facilities Council. This research has benefitted from the SpeX Prism Spectral Libraries, maintained by Adam Burgasser at <http://pono.ucsd.edu/~adam/browndwarfs/spexprism>. RB would like to thank L. Barnett-Kramp for useful comments on an early draft of the paper.

DATA AVAILABILITY

This work is based on the VIKING data release VIKINGv20160406 available as part of the VISTA Science Archive (<http://horus.roe.ac.uk/vsa/index.html>). A version of the BMC code is publicly available at http://github.com/rhysrb/Pq_server. Raw ESO follow-up data can be accessed via <http://archive.eso.org/cms.html> as part of programme 0102.A-0848(A). Derived data products generated in this research will be shared on reasonable request to the corresponding author.

REFERENCES

Atek H., et al., 2011, *ApJ*, 743, 121

Barnett R., Warren S., Becker G., Mortlock D., Hewett P., McMahon R., Simpson C., Venemans B., 2017, *A&A*, 601, A16

Bochanski J. J., Hawley S. L., Covey K. R., West A. A., Reid I. N., Golimowski D. A., Ivezić Ž., 2010, *AJ*, 139, 2679

Bruzual G., Charlot S., 2003, *MNRAS*, 344, 1000

Chambers K. C., et al., 2016, arXiv e-prints, p. arXiv:1612.05560

Chen S.-F. S., et al., 2017, *ApJ*, 850, 188

Cross N. J. G., et al., 2012, *A&A*, 548, A119

Cross N., Collins R., Read M., Blake R., Sutorius E., Hambly N., Holliman M., Mann R., 2014, in Manset N., Forshay P., eds, *Astronomical Society of the Pacific Conference Series Vol. 485, Astronomical Data Analysis Software and Systems XXIII*. p. 371, <http://adsabs.harvard.edu/abs/2014ASPC...485...371C>

Decarli R., et al., 2017, *Nature*, 545, 457

Decarli R., et al., 2018, *ApJ*, 854, 97

Dey A., et al., 2019, *AJ*, 157, 168

Dupuy T. J., Liu M. C., 2012, *ApJS*, 201, 19

Edge A., Sutherland W., Kuijken K., Driver S., McMahon R., Eales S., Emerson J. P., 2013, *The Messenger*, 154, 32

Euclid Collaboration 2019, *A&A*, 631, A85

Fan X., et al., 2019, *ApJ*, 870, L11

Hall P. B., et al., 2002, *ApJS*, 141, 267

Hayashi M., et al., 2018, *PASJ*, 70, S17

Hewett P. C., Warren S. J., Leggett S. K., Hodgkin S. T., 2006, *MNRAS*, 367, 454

Jarvis M. J., et al., 2013, *MNRAS*, 428, 1281

Jiang L., et al., 2016, *AJ*, 833, 222

Koptelova E., Hwang C.-Y., Yu P.-C., Chen W.-P., Guo J.-K., 2017, *Scientific Reports*, 7, 41617

Laigle C., et al., 2016, *ApJS*, 224, 24

Maddox N., Hewett P. C., Warren S. J., Croom S. M., 2008, *MNRAS*, 386, 1605

Marshall H. L., Tananbaum H., Avni Y., Zamorani G., 1983, *ApJ*, 269, 35

Matsuoka Y., et al., 2016, *ApJ*, 828, 26

Matsuoka Y., et al., 2018a, *PASJ*, 70, S35

Matsuoka Y., et al., 2018b, *ApJS*, 237, 5

Matsuoka Y., et al., 2019, *ApJ*, 872, L2

Mortlock D. J., et al., 2011, *Nature*, 474, 616

Mortlock D. J., Patel M., Warren S. J., Hewett P. C., Venemans B. P., McMahon R. G., Simpson C., 2012, *MNRAS*, 419, 390

Pipien S., Cuby J. G., Basa S., Willott C. J., Cuillandre J. C., Arnouts S., Hudelot P., 2018, ArXiv e-prints: 1808.10672

Pons E., McMahon R. G., Simcoe R. A., Banerji M., Hewett P. C., Reed S. L., 2019, *MNRAS*, 484, 5142

Reed S. L., et al., 2017, *MNRAS*, 468, 4702

Reed S. L., et al., 2019, *MNRAS*, 487, 1874

Ross N. P., Cross N. J. G., 2020, *MNRAS*, 494, 789

Shanks T., et al., 2015, *MNRAS*, 451, 4238

Skrutskie M. F., et al., 2006, *AJ*, 131, 1163

Skrzypek N., Warren S. J., Faherty J. K., Mortlock D. J., Burgasser A. J., Hewett P. C., 2015, *A&AS*, 574, A78

Skrzypek N., Warren S. J., Faherty J. K., 2016, *A&AS*, 589, A49

Songaila A., Hu E. M., Barger A. J., Cowie L. L., Hasinger G., Rosenwasser B., Waters C., 2018, *ApJ*, 859, 91

Stephens D., Leggett S., 2004, *PASP*, 116, 9

Tang J.-J., et al., 2017, *MNRAS*, 466, 4568

Venemans B. P., et al., 2013, *ApJ*, 779, 24

Venemans B. P., et al., 2015a, *MNRAS*, 453, 2259

Venemans B. P., et al., 2015b, *ApJ*, 801, L11

Wang F., et al., 2017, *ApJ*, 839, 27

Wang F., et al., 2019, *ApJ*, 884, 30

West A. A., et al., 2011, *AJ*, 141, 97

Willott C. J., et al., 2010, *AJ*, 139, 906

Yang J., et al., 2019, *AJ*, 157, 236

Yang J., et al., 2020, *ApJ*, 897, L14

de Jong J. T. A., et al., 2017, *A&A*, 604, A134

van der Wel A., et al., 2014, *ApJ*, 788, 28

APPENDIX A: PRIMARY AND SECONDARY OBSERVATIONS IN VIKING

The basic VISTA survey area is, as described by Cross et al. (2012), a ‘tile’ (which we have also referred to as a frameset in this work), formed of six individual exposures labelled ‘pawprints’. These pawprints are offset such that a single tile is at least doubly exposed, with the exception of a narrow strip at the top and bottom of the tile, which is imaged just once. These strips overlap with adjacent tiles, allowing the minimum survey depth to be achieved by ensuring the full VIKING area is imaged at least twice. A consequence of this observation strategy is that duplicate entries appear in the table. After source merging is complete, a process known as seaming takes place, which identifies and flags duplicates, using the PriOrSec (POS) property.

Where a VIKING source is duplicated, the ‘better’ entry as determined on the basis of the proximity to the optical axis of the camera, is labelled as the primary using the POS flag, and the other entry labelled the secondary. Our list-driven catalogue contains 4.3×10^7 entries, of which 18% are labelled as secondary. This proportion corresponds closely to the area of a tile that is singly imaged (Cross et al. 2012).

Given that such a large proportion of VIKING sources are duplicated, in our search for HZQs using the BMC method we applied slightly different criteria to these doubly-observed sources to avoid missing any interesting candidates. If either of the primary or secondary observations of a doubly-observed source satisfied $P_q > 0.1$, we averaged the primary and secondary photometry using inverse variance weighting, and assessed its selection again, this time applying the $P_q > 0.15$ threshold. Two known quasars (for which both the primary and secondary entries satisfied $P_q > 0.15$ anyway) and two of the new candidates, indicated in Table 1, were selected in this way.

We also assessed the impact of primaries/secondaries on our BMC HZQ selection function. The flux errors of the VIKING secondaries are typically somewhat worse than the primary flux errors, up to a level of 30%. For each HZQ that we simulate (representing primaries), we therefore produce a second set of photometry drawn from flux distributions with the uncertainties enhanced by 30% (secondaries). Again, if either the primary or secondary HZQ entry was selected using the relaxed criteria, we produced a third set of photometry for each HZQ, by averaging the primary and secondary photometry using inverse variance weighting. We find, for a simulated HZQ, selection using the combined photometry matches selection using only primary data very closely. We conclude that the presence of a secondary does not typically allow the selection of a source that is not otherwise selected, nor does it prevent the selection of a HZQ that is selected on the basis of its primary.

APPENDIX B: POPULATION MODELLING

Here we summarise the surface density terms and model colours which are used in the selection methods described in Sect. 3. We present the models for quasars in Sect. B1, for MLTs in Sect. B2, and for ETGs in Sect. B3. The population models are determined following the same procedures detailed in *Euclid* Collaboration (2019), allowing for the differences between the *Euclid* and VIKING filters, and the different image quality, which is relevant to modelling the ETGs. We therefore provide a shorter outline in the following sections, but draw attention to aspects of the population models that differ from the *Euclid* work. The model colours are shown in Fig. 2. As a reminder, in this paper magnitudes are quoted on the Vega sys-

tem, whereas in *Euclid* Collaboration (2019) they are on the AB system.

B1 Quasars

The parameters θ for the quasars are absolute magnitude and redshift. For the VIKING analysis we adopt the single power law QLF used by Mortlock et al. (2012), since we do not probe significantly fainter than the “knee” of the luminosity function (Jiang et al. 2016). The redshift evolution of this QLF uses $k = -0.47$: we have not adopted the stronger values since we started selecting VIKING quasar candidates before Jiang et al. (2016) or Wang et al. (2019) were published. While using a weaker evolution for the quasar weight will boost the resulting values of P_q , the relative probabilistic ranking of VIKING sources will be almost unchanged; even using a more strongly evolving QLF we could select almost exactly the same list of candidates by adjusting the P_q threshold.

As was the case in *Euclid* Collaboration (2019), we use *synphot* to directly measure the quasar k -corrections and colours used in the SED fitting and BMC techniques, from updated versions of the model spectra from Hewett et al. (2006) and Maddox et al. (2008). We use the version of the model with ‘standard’ continuum slope and emission line strength in the selection. For our simulated sources we assume that all flux blueward of $\text{Ly}\alpha$ is absorbed, except that we include a near zone of radius 3 Mpc (proper). Our quasar selection functions are not sensitive to the choice of the near zone size. The decision to use only one model for selection was taken early on in the project, at a time when the new multi-population selection algorithm was being developed. In hindsight it would have been better to include a range of quasar models in the candidate selection. This point is discussed in *Euclid* Collaboration (2019), where we estimate that the quasar yield could be $\sim 20\%$ higher.

B2 MLT dwarfs

The total MLT weight is determined by summing individual sub-weights, computed for each spectral type M0–T8. We therefore require the full range of VIKING $ZYJHK_s$ colours for each spectral type. Skrzypek et al. (2015, 2016) provide UKIDSS $YJHK$ colours for types M7–T8. The UKIDSS YJH filters are a close match to VISTA; however, there is no match in those works for the VISTA Z and K_s bands, so $Z - Y$ and $H - K_s$ must be determined separately for M7–T8. We additionally require the full set of VIKING colours for M0–M6. To proceed, we select a bright subsample ($S/N_i > 50$) from the spectroscopic M dwarf catalogue presented by West et al. (2011). We determine average $Z - Y$ and $H - K_s$ colours for all M dwarfs by matching the M dwarf sample to VIKING. We additionally match the M dwarf sample to UKIDSS and measure median $rizYJH$ SDSS/UKIDSS colours for M0–M5. These are required for the M0–M5 absolute magnitudes, as detailed further below.

For the L and T dwarf $H - K_s$ colour we make use of the corrections provided by Stephens & Leggett (2004), which allow conversions between the MKO filter set used by UKIDSS, and other photometric systems. We find the DENIS K band provides a close match to the VIKING K_s filter, allowing us to approximate $H - K_s$ for L and T types. Finally, we determine $Z - Y$ colours for L and T dwarfs by fitting a polynomial to the sources presented by Hewett et al. (2006). We present the full set of VIKING $ZYJHK_s$ colours in Table B1.

The dwarf star surface density term requires number densities and absolute magnitudes for each spectral type. We use the the Galactic plane number densities presented in *Euclid* Collaboration (2019).

Table B1. MLT density and model colour data for VIKING.

SpT	ρ_0 (pc $^{-3}$)	M_J	$Z - Y$	$Y - J$	$J - H$	$H - K_s$
M0	2.4×10^{-3}	5.69	0.29	0.45	0.62	0.19
M1	2.7×10^{-3}	6.24	0.32	0.47	0.60	0.22
M2	4.4×10^{-3}	6.85	0.35	0.49	0.58	0.23
M3	7.8×10^{-3}	7.38	0.39	0.51	0.55	0.24
M4	1.0×10^{-2}	7.96	0.44	0.53	0.54	0.26
M5	1.1×10^{-2}	8.56	0.51	0.57	0.53	0.29
M6	7.8×10^{-3}	9.86	0.60	0.63	0.53	0.31
M7	2.2×10^{-3}	10.65	0.70	0.68	0.54	0.34
M8	1.7×10^{-3}	11.06	0.83	0.79	0.56	0.38
M9	1.1×10^{-3}	11.31	0.99	0.87	0.59	0.42
L0	6.7×10^{-4}	11.52	1.20	1.04	0.63	0.53
L1	4.3×10^{-4}	11.78	1.29	1.11	0.67	0.55
L2	3.8×10^{-4}	12.11	1.33	1.18	0.73	0.59
L3	3.6×10^{-4}	12.51	1.36	1.23	0.79	0.62
L4	5.3×10^{-4}	12.95	1.38	1.27	0.86	0.66
L5	4.1×10^{-4}	13.40	1.40	1.31	0.91	0.68
L6	2.2×10^{-4}	13.82	1.42	1.33	0.96	0.70
L7	6.3×10^{-4}	14.17	1.46	1.35	0.97	0.70
L8	3.9×10^{-4}	14.42	1.51	1.21	0.96	0.68
L9	4.8×10^{-4}	14.56	1.59	1.20	0.90	0.63
T0	6.3×10^{-4}	14.60	1.69	1.19	0.80	0.55
T1	6.4×10^{-4}	14.55	1.82	1.19	0.65	0.45
T2	3.6×10^{-4}	14.45	1.97	1.18	0.46	0.33
T3	3.6×10^{-4}	14.35	2.14	1.18	0.25	0.19
T4	5.6×10^{-4}	14.32	2.32	1.17	0.02	0.06
T5	7.1×10^{-4}	14.44	2.52	1.16	−0.19	−0.05
T6	2.1×10^{-4}	14.78	2.72	1.16	−0.35	−0.12
T7	2.1×10^{-3}	15.42	2.92	1.15	−0.43	−0.11
T8	7.5×10^{-4}	16.42	3.10	1.15	−0.36	0.01

Dupuy & Liu (2012) provide MKO J -band absolute magnitudes for spectral types M6–T8. For M0–M5 we use the relationship between $i - z$ and M_r from Bochanski et al. (2010). We correct to the Vega system using the offsets provided by Hewett et al. (2006), and then use the colours determined above to convert M_r to M_J . As in *Euclid* Collaboration (2019), we have assumed MLT number density varies as $\rho = \rho_0 e^{-Z/Z_s}$, where ρ_0 is the number density of any spectral type M0–T8 at the Galactic central plane, Z is the vertical distance from the plane, and Z_s is the scale height, assumed to be 300 pc. The small offset of the Sun from the Galactic plane is disregarded.

B3 Early-type galaxies

Over the redshift range $z = 1 - 2$, ETGs have red NIR colours, which can resemble the colours of high-redshift quasars at low S/N. In previous works, which have focused on the brightest candidates, this source of contamination has been mitigated by taking a cut on a morphological statistic (e.g., Mortlock et al. 2012; Venemans et al. 2013). However, size and stellar mass for the ETG population are strongly correlated (van der Wel et al. 2014), suggesting faint early-type galaxies at these redshifts will be very compact, and classified as point sources by VIKING. We illustrate this point in Fig. B1, which shows the behaviour of the MCS statistic as a function of J magnitude for our initial sample of red sources, before applying the cut on MCS (see Sect 3.1). At bright magnitudes ($J \lesssim 19$), there are two distinct populations: point sources, with $\text{MCS} \approx 0$, and extended sources at much higher values. However, at fainter magnitudes, the two populations become merged, i.e., morphology is no longer a good discriminator. We therefore have to incorporate the ETG population as a contaminant.

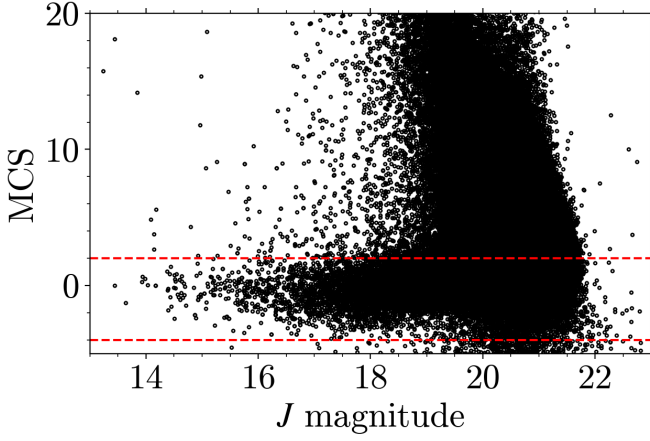


Figure B1. MCS statistic as a function of J magnitude. Black points mark the sources in our VIKING sample, where we have not taken a cut on MCS. The red dashed lines indicate our cut to eliminate bright ellipticals.

We firstly derive a model for the surface density and colours of ETGs as a function of redshift and J magnitude. We then account for the magnitude dependence of the MCS parameter. As in [Euclid Collaboration \(2019\)](#), we make use of the COSMOS/UltraVISTA sources presented by [Laigle et al. \(2016\)](#) to derive the model. [Euclid Collaboration \(2019\)](#) found that quiescent objects in the COSMOS catalogue have a large range of formation redshifts (z_f), approximating the catalogue as two separate populations, with a fraction 0.8 having $z_f = 3$, and a fraction 0.2 having $z_f = 10$. We use colours computed for both formation redshifts, from the evolutionary models of [Bruzual & Charlot \(2003\)](#).

To produce a surface density model that can be applied to VIKING, we first fit a surface density model to $2''.0$ aperture COSMOS data. We then require corrections to convert COSMOS aperture magnitudes to VIKING APERMAG3 magnitudes. The COSMOS/UltraVISTA area does not overlap with VIKING; however, there is overlap with the UKIDSS LAS, and the UKIDSS and VIKING data are similar in terms of image quality and the data-processing pipeline. We find 195 COSMOS sources are detected in the K band in the LAS, allowing us to compare the $2''.0$ aperture magnitudes between the LAS and COSMOS. The UKIDSS APERMAG3 photometry corresponds to the flux in a $2''.0$ aperture, that is then aperture corrected to total flux using the aperture correction for a point source. Therefore the aperture correction has to be subtracted to get the LAS flux in the $2''.0$ aperture. After doing this we find the UKIDSS fluxes agree with the COSMOS fluxes almost exactly, on average. On this basis we use the following relation between the $2''.0$ aperture J -band AB COSMOS magnitudes J_{corr} and VIKING Vega APERMAG3 J magnitudes: $J_{\text{corr}} = J + 1.147$. This equation incorporates both the AB correction and the point source aperture correction.

The surface density function in terms of J_{corr} and source redshift is determined from a maximum likelihood fit. The functional form of this function in units of $\text{mag}^{-1} \text{deg}^{-2}$ per unit redshift is

$$\Sigma(J_{\text{corr}}, z) = \alpha \exp \left\{ -\frac{1}{2} \left[\frac{J_{\text{corr}} - (J_0 + bz)}{\sigma} \right]^2 \right\} \exp \left[-\left(\frac{z - 0.8}{z_0} \right) \right] \quad (\text{B1})$$

where we find the best-fitting parameters to be $(\alpha, \sigma, J_0, b, z_0) = (7697, 0.883, 20.467, 1.462, 0.429)$. We assume the same function is

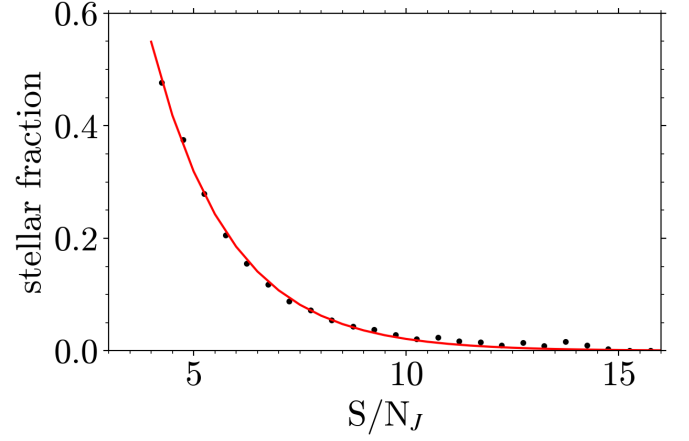


Figure B2. Measured fraction of ETGs classified as stellar as a function of S/N_J . The red curve shows the exponential fit, Eq. B2.

applicable to early-type galaxies with either formation redshift, and scale the resulting weights by 0.8 for $z_f = 3$ and 0.2 for $z_f = 10$ to reflect the distribution of z_f values seen in the COSMOS data.

The surface density function and the model colours provide a complete description of the ETG population, with the exception that only objects satisfying the cut $-4 < \text{MCS} < 2$ will appear in the sample. We therefore need to quantify the magnitude dependence of this cut on MCS. We wish to evaluate the fraction of ETGs that satisfy the MCS cut. From the counts of red sources as a function of S/N we can tally separately stellar sources, with $-4 < \text{MCS} < 2$, and extended sources. We can subtract the counts of MLTs from the stellar counts using the density model for these sources. Then we are left with galaxy counts only as a function of S/N , separated into galaxies classified as stellar and galaxies classified as extended. The proportion of galaxies classified as stellar as a function of S/N in the J band is plotted in Fig. B2. The resulting function is well fit by an exponential of the form

$$\text{stellar fraction} = a \cdot \exp(-b \cdot S/N_J), \quad (\text{B2})$$

where we find the best fit to be $(a, b) = (4.837, 0.544)$. The full galaxy prior is formed by multiplying Equations B1 and B2.

APPENDIX C: SIMULATING DETECTION IN THE J BAND

Our list-driven sample starts with the list of objects detected in the original VIKING catalogue which have $S/N > 4$ in an aperture of diameter $2''.0$. For a source in the J band that has a given S/N in the aperture, we want to know the probability that it would have been detected, i.e., would have made it into the VIKING catalogue. We cannot measure this in the J band itself since we do not have measurements of the sources not in the VIKING catalogue. However, whether or not a source in, say, the Y band measured at a particular S/N gets into the VIKING catalogue does not depend on what happens in the J band. So we can gauge the detection probability in any chosen band starting with any catalogue of real sources detected in some other band, and then measuring them in the chosen band.

We start by matching a sample of sources classified as stellar in the deeper VISTA Deep Extragalactic Observations survey (VIDEO; [Jarvis et al. 2013](#)) survey to our list-driven catalogue. This simply ensures that the objects are real, since they are found in both catalogues.

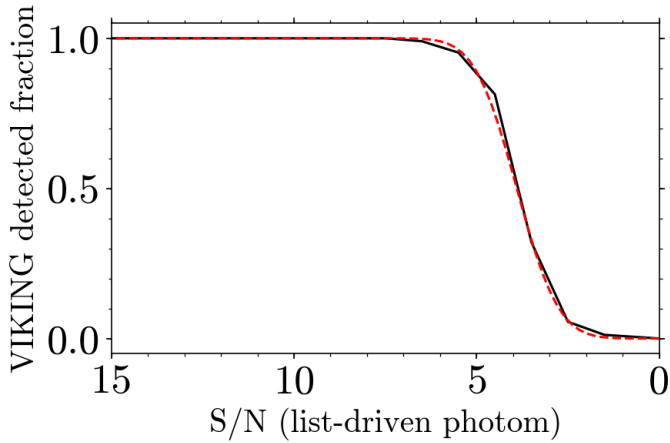


Figure C1. VIKING completeness as a function of S/N in any band. Results from the Y , H and K_s bands have been averaged. The red dashed line plots the cumulative Gaussian function that we fit to the data.

Then in, e.g., the Y band, we evaluate the fraction of sources that are detected in Y in VIKING (i.e., appear in the original VIKING catalogue) as a function of S/N in the aperture in that band. The results averaged over the Y , H , and K_s bands are plotted in Fig. C1.

To be clear, this says that if an object has the given S/N in the aperture on any frame, then the probability that it will appear in the original VIKING catalogue is given by the function plotted. This is the function needed to quantify detection in the J band for modelling the selection functions (Sect. 5), and for creating the synthetic catalogue (Sect. 6). We fit a Gaussian cumulative distribution function (CDF; i.e., the error function) to this curve. The (50,68,95)% quantiles are found to lie at at $S/N = (3.9, 4.8, 5.7)$. Each source that we simulate is then detected or rejected with a probability set by this CDF, leaving us with sources that would be present in the VIKING list-driven catalogue.

This paper has been typeset from a \LaTeX file prepared by the author.